

# Noninvasive Vascular Elastography: Theoretical Framework

Roch L. Maurice, Jacques Ohayon, Yves Frétnigny, Michel Bertrand, Gilles Soulez, and Guy Cloutier\*

**Abstract**—Changes in vessel wall elasticity may be indicative of vessel pathologies. It is known, for example, that the presence of plaque stiffens the vascular wall, and that the heterogeneity of its composition may lead to plaque rupture and thrombosis. Another domain of application where ultrasound elastography may be of interest is the study of vascular wall elasticity to predict the risk of aneurysmal tissue rupture. In this paper, this technology is introduced as an approach to noninvasively characterize superficial arteries. In such a case, a linear array ultrasound transducer is applied on the skin over the region of interest, and the arterial tissue is dilated by the normal cardiac pulsation. The elastograms, the equivalent elasticity images, are computed from the assessment of the vascular tissue motion. Investigating the forward problem, it is shown that motion parameters might be difficult to interpret; that is because tissue motion occurs radially within the vessel wall while the ultrasound beam propagates axially. As a consequence of that, the elastograms are subjected to hardening and softening artefacts, which are to be counteracted. In this paper, the Von Mises (VM) coefficient is proposed as a new parameter to circumvent such mechanical artefacts and to appropriately characterize the vessel wall. Regarding the motion assessment, the Lagrangian estimator was used; that is because it provides the full two-dimensional strain tensor necessary to compute the VM coefficient. The theoretical model was validated with biomechanical simulations of the vascular wall properties. The results allow believing in the potential of the method to differentiate hard plaques and lipid pools from normal vascular tissue. Potential *in vivo* implementation of noninvasive vascular elastography to characterize abdominal aneurysms and superficial arteries such as the femoral and the carotid is discussed.

**Index Terms**—Mathematical modeling, mechanical properties, noninvasive scanning, ultrasound elastography, vascular pathologies, vascular wall.

## I. INTRODUCTION

**P**ATHOLOGICAL conditions often induce changes in biological tissue stiffness. That is, for example, the basic hypothesis supporting palpation as a screening method to detect hard tumors in the breast, prostate and other organs. However, in many instances, such an approach is impracticable when deep organs are considered. This gave rise to elasticity imaging, which aims to outline the elastic properties of biological soft tissues using ultrasound.

In the early nineties, Ophir *et al.* [1] introduced elastography, which is defined as biological tissue elasticity imaging. Primary objectives of elastography were to complement B-mode ultrasound as a screening method to detect hard areas in the breast [2], [3], and to investigate prostate cancers [4], [5]. Such approaches are sometimes referred to as *computed palpation*. Basically, the tissue under inspection is externally compressed and the displacement between pairs of precompression and postcompression radio frequency (RF) lines is estimated using cross-correlation analysis. The strain profile in the tissue is then determined from the gradient of the axial displacement field.

Elastography has also found application in vessel wall characterization. Until now, vascular elastography is invasive and is known in the literature as intravascular ultrasound (IVUS) elastography or, sometimes, as endovascular elastography (EVE). In EVE, the vascular tissue is compressed by applying a force from within the lumen. Indeed, the compression can be induced by the normal cardiac pulsation or by using a compliant intravascular angioplasty balloon. Such a balloon may also be used to stabilize the EVE catheter position in the lumen. This approach can be seen as a complement to B-mode IVUS.

### A. Reported Works on EVE (Relevant to the Current Study)

*1) Simulations and Phantom Studies:* One of the first investigations on EVE was presented by Soualmi *et al.* [6] in 1997. Indeed, they used finite element analysis to better understand the vessel wall elasticity images. To validate the feasibility of EVE, phantom studies have been proposed. In most cases, tissue-mimicking phantoms with typical morphology and hardness topology synthesizing atherosclerotic vessels were constructed. de Korte *et al.* [7] concluded that EVE may allow identifying hard and soft plaques independently of the echogeneity contrast between the plaque and the vessel wall. The potential

Manuscript received March 12, 2003; revised August 26, 2003. The work of G. Cloutier was supported in part by the Natural Sciences and Engineering Research Council of Canada under Grant 138570-01. The work of J. Ohayon, M. Bertrand, G. Soulez, and G. Cloutier was supported in part by the Valorisation-Recherche Québec structuring group program. The work of M. Bertrand and G. Cloutier was supported in part by the Quebec Ministry of Education FCAR group program. A part of the project upon which this publication is based was performed pursuant to the University of Texas Grant CA64597 (M. Bertrand) with the NIH, PHS. The salaries of G. Soulez and G. Cloutier are supported in part by research scholarship awards from the Fonds de la Recherche en Santé du Québec. The Associate Editor responsible for coordinating the review of this paper and recommending its publication was G. Wang. Asterisk indicates corresponding author.

R. L. Maurice, Y. Frétnigny, and G. Cloutier are with the Laboratory of Biorheology and Medical Ultrasonics, Research Center, University of Montreal Hospital, Montreal, Quebec H2L 2W5, Canada.

J. Ohayon is with the Laboratory TIMC-IMAG, UMR CNRS 5525, Institut A. Bonniot, 38706 La Tronche, France.

M. Bertrand is with the Institute of Biomedical Engineering, École Polytechnique, University of Montreal, Montreal, Quebec H3C 3A7, Canada.

G. Soulez is with the Department of Radiology, University of Montreal Hospital, Montreal, Quebec H2L 4M1, Canada.

\*G. Cloutier, Director, Laboratory of Biorheology and Medical Ultrasonics, Research Center, University of Montreal Hospital, 2099 Alexandre de Sève (room Y-1619), Montréal, Québec H2L 2W5, Canada (e-mail: guy.cloutier@umontreal.ca).

Digital Object Identifier 10.1109/TMI.2003.823066

of such an approach was emphasized by the fact that it provides information that may be unavailable from IVUS alone.

*In vivo*, the position of the catheter in the lumen is normally off center, and the geometry of the lumen is generally not circular. In such cases, tissue displacements may be misaligned with the ultrasound beam, introducing substantial decorrelation between the precompression and the postcompression signals. As to prevent such limitations, Ryan and Foster [8] proposed the use of a two-dimensional (2-D) correlation-based speckle tracking method to compute vascular elastograms. While questioning the limitations of the lateral tracking performance, they concluded their phantom studies claiming that EVE may provide a new spectrum of information to aid in the assessment of atherosclerotic lesions.

Additionally, *in vivo*, the catheter may cyclically move in the lumen because of the pulsatile blood flow motion. This constitutes another potential source of decorrelation for the precompression and the postcompression signal treatment. To counteract that, Shapo *et al.* [9], [10] proposed to compute the tissue motion in the reference frame of the lumen's geometric center of the angioplasty balloon. Such a reference frame depends only on the balloon shape; it, thus, removes artefacts associated with probe motion within the balloon. Their phantom investigations also tended to demonstrate the feasibility of EVE and its potential to differentiate between hard and soft plaques.

More recent results on endovascular phantom studies were obtained by Brusseau *et al.* [11]. Instead of the traditional correlation-based methods, they used an iterative approach to compute a scaling factor between precompression and postcompression signal segments. From that, the strain was estimated. This adaptive method is expected to be accurate in a wider range of strains than the commonly used gradient-based methods, and it may prove better for investigating highly heterogeneous tissues.

2) *In Vitro Studies With Excised Vessels*: One more step to validate the feasibility of EVE is *in vitro* experiments. de Korte *et al.* [12], [13] computed elastograms from diseased human femoral and coronary arteries. They found different strain values between fibrous, fibro-fatty and fatty plaques, indicating the potential of EVE to distinguish different plaque constituents. Such results were compared with IVUS echograms and corroborated with histology. One of their principal findings was that the elastograms were capable of demarcating regions within the plaque representing differences in strain, whereas in IVUS echograms, these regions could not be discriminated. Using excised post-mortem carotid arteries, similar results were recently observed by Brusseau *et al.* [11].

*In vitro* EVE also was conducted by Wan *et al.* [14]. They used an algorithm-based optical flow method to estimate the displacement from B-mode data collected from porcine arteries. They also computed the elasticity modulus distributions within the framework of the inverse-problem solution (estimation of the Young's modulus). While low spatial resolution of envelope data remains a limitation, the method seemed encouraging because of the highest accessibility of B-mode compared to RF instrumentation.

3) *In Vivo Studies*: Currently, *in vivo* applications of EVE are scarce. de Korte *et al.* [15] attempted to compute elastograms

*in vivo* from patients referred to percutaneous coronary intervention. Indeed, as preintervention IVUS assessment of the lesions was performed, RF data were acquired to compute elastograms. To minimize artefacts due to catheter motion, pre-tissue-motion and post-tissue-motion images were acquired near end-diastole; that is for a pressure differential of approximately 5 mmHg. One elastogram was presented; it identified an area as being composed of hard material since low strain values were found. Such a finding was corroborated with the IVUS echograms that revealed a large calcified area. That result allows believing in the potential of EVE for follow-up of patients with vascular diseases.

## B. Noninvasive Vascular Elastography (NIVE)

So far, vascular elastography is invasive. Its clinical application is, thus, restricted to a complementary tool to assist IVUS echograms in preoperative lesion assessments and to plan endovascular therapy. It has also found application in *in vitro* studies to characterize vascular tissues. Nevertheless, elastography is a very attractive and promising approach to characterize the mechanical properties of vascular walls. In this paper, the feasibility of noninvasive vascular elastography is investigated.

In the next sections, the Lagrangian estimator [16], [17] and its implementation for vessel wall characterization are summarized. The full 2-D strain tensor  $\epsilon$  is provided, but the so-called elastogram is given by the strain component  $\epsilon_{yy}$ , which corresponds to the strain in the direction of the ultrasound propagation. Investigating the forward problem (FP), it is shown in Section II that such an elastogram is subjected to hardening and softening artefacts; that is explained by the fact that motion occurs radially within the vessel wall while the ultrasound beam propagates axially. To circumvent such incoherence, the Von Mises (VM) coefficient is proposed as a new parameter to noninvasively characterize the vessel wall. Results from biomechanical simulations of wall tissue displacement validate the potential of the approach to accurately differentiate hard plaques and lipid pools from the normal vascular tissue. Potential *in vivo* implementation of noninvasive vascular elastography to characterize abdominal aneurysms and superficial arteries, such as the femoral and the carotid, is discussed in Section IV.

## II. METHODOLOGY

In conventional elastography, an axial compression is applied so that the tissue motion occurs in the ultrasound beam axis. In such a case, a one-dimensional (1-D) estimator can provide reliable tissue motion assessment. In some circumstances, 2-D companding [18], [19] may be required to compensate for non-axial motion. In NIVE, the challenge stems from the fact that motion occurs radially within the vessel wall section while the ultrasound beam propagates axially (linear array transducers are considered in the present study). Regarding that, 1-D estimators are not appropriate. In this paper, the Lagrangian speckle model estimator (LSME) is, thus, proposed to noninvasively characterize vascular tissues. Indeed, the LSME is a 2-D model-based estimator that allows computing the full 2-D-strain tensor [16].

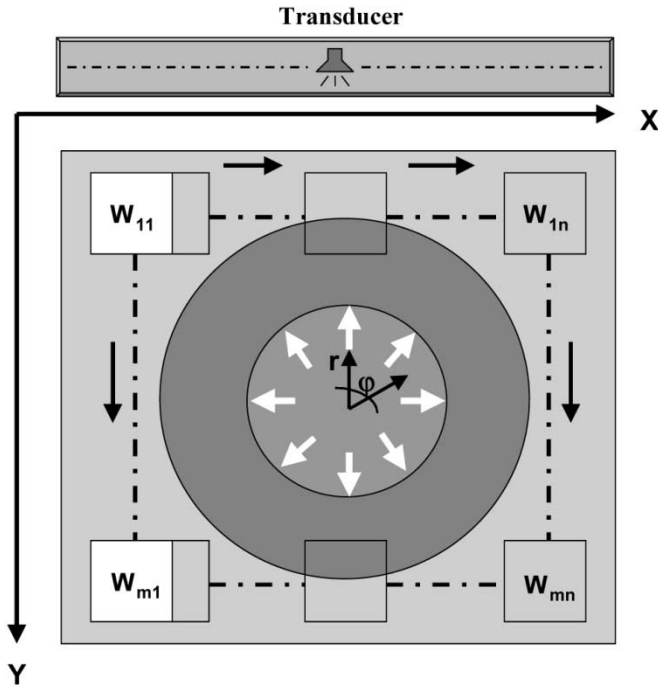


Fig. 1. Simplified illustration of NIVE acquisition system, showing that the tissue motion occurs radially, whereas the linear-array transducer scans in the Cartesian coordinate system. Processing motion estimation requires 2-D segmentation of the images; the  $W_{mn}$  represent the data windows that are used by the LSME.

The approach relies on a tissue-motion model and on a dynamic image-formation model that are summarized in the next sections.

#### A. The Tissue-Motion Model

Subjected to blood flow pressure, the apparent motion of an artery is dilation; however, because of the boundary conditions imposed by the surrounding tissues and organs, the vascular wall itself is compressed. Such a compression induces a radial strain that is maximum at the inner wall and minimum at the outer wall; this observation is referred to, in the literature, as the strain decay. However, as illustrated in Fig. 1, motion occurs radially in NIVE and is parallel to the ultrasound beam only at angles  $\varphi$  of  $0^\circ$  and  $180^\circ$  (note that cross-sectional images are considered here). Moreover, the vascular tissue is heterogeneous; it is, thus, expected to deform nonuniformly. Accordingly, proceeding to motion estimation requires subdividing the region under study into several 2-D sub-regions of interest (ROIs). This is shown in Fig. 1, where the ROIs are represented by the measurement-windows  $W_{mn}$ .

For small ROIs ( $W_{mn}$ ), tissue motion can be approximated by the zero-order and first-order terms of a Taylor-series expansion; this can be expressed as

$$\begin{bmatrix} p(x, y, t) \\ q(x, y, t) \end{bmatrix} = \underbrace{\begin{bmatrix} \theta_1 \\ \theta_4 \end{bmatrix}}_{\text{Tr}} + \underbrace{\begin{bmatrix} \theta_2 & \theta_3 \\ \theta_5 & \theta_6 \end{bmatrix}}_{\text{LT}} \begin{bmatrix} x \\ y \end{bmatrix} \quad (1)$$

where  $\theta_i$  is a function of time  $t(\theta_i(t))$ . Equation (1) defines an affine transformation, i.e., it is the result of a translation (vector  $[\text{Tr}]$ ) and of a linear geometrical transformation of coordinates

(matrix  $[\text{LT}]$ ). Equation (1) can also be seen as trajectories that describe a tissue motion in a region of constant strain [16]. Strain is usually defined in terms of the gradient of a displacement field; hence, as  $p(x, y, t)$  and  $q(x, y, t)$  represent the new position of a point  $(x, y)$ , the  $(u, v)$  components of the displacement vector in the  $(x, y)$  system are given by

$$\begin{bmatrix} u \\ v \end{bmatrix} = \begin{bmatrix} p(x, y, t) - x \\ q(x, y, t) - y \end{bmatrix} = \begin{bmatrix} \theta_1 \\ \theta_4 \end{bmatrix} + \Delta \begin{bmatrix} x \\ y \end{bmatrix}$$

(2)

with :  $\Delta = \begin{bmatrix} \theta_2 - 1 & \theta_3 \\ \theta_5 & \theta_6 - 1 \end{bmatrix}$ .

The  $\varepsilon_{ij}$ , which are the components of the strain tensor  $\varepsilon$ , can then be defined in terms of the  $\theta$  parameters as

$$\varepsilon_{ij}(t) = \frac{1}{2} [\Delta_{ij}(t) + \Delta_{ji}(t)]. \quad (3)$$

For an ultrasound pulse propagating in the  $y$ -axis direction,  $\varepsilon_{xx}$  and  $\varepsilon_{yy}$  represent, respectively, the lateral and the axial strains;  $\varepsilon_{xy} = \varepsilon_{yx}$  is the shear strain. Because conventional elastography assumes a constant stress distribution in the ROI, the axial strain is inversely proportional to the Young's modulus. Accordingly  $\varepsilon_{yy}$ , known in the literature as the elastogram, can be seen as a map of the tissue stiffness. In other words, elastography may allow identifying different tissue structures such as hard plaques and lipid pools, or heterogeneity in the aneurysmal vessel wall.

#### B. The Dynamic Image-Formation Model

It is assumed that the image formation can be modeled as a linear space-invariant operation on a scattering function. If it is further assumed that the motion occurs in plane strain conditions (that is no transverse motion is involved), then the following simple 2-D model can be used [20], [21]

$$I(x, y) = H(x, y) \otimes Z(x, y) \quad (4)$$

where  $I(x, y)$  is the RF image,  $H(x, y)$  is the point-spread function (PSF) of the ultrasound system,  $\otimes$  is the 2-D convolution operator, and  $Z(x, y)$  is the acoustic impedance function, which can be modeled as a white Gaussian noise (random distribution of scatterers within the ROI).

Let us now derive the 2-D dynamic image-formation model for an in-plane tissue motion. For small ROIs such as in Fig. 1, motion impressed on the tissue  $[Z(x, y)]$  can be assumed an affine transformation [see (1)]. This means that such a motion can be set by only changing the  $(x, y)$  coordinates. Without loss of generality, it is assumed that the translation  $[\text{Tr}]$  is absent (no rotation of the blood vessel during pulsation) or is appropriately compensated for and can, thus, be neglected. The compensation for translation can be done using correlation techniques; such a processing is known, in the literature, as *companding* [18]. It is also interesting to notice that impress  $[\text{LT}]$  on the tissue requires to compute the inverse transformation  $[\text{LT}^{-1}]$  on the coordinates. Hence, for an  $(x, y)$  in-plane motion, the 2-D RF dynamic image-formation model is given by

$$I(x, y, t) = H(x, y) \otimes Z_{\text{LT}^{-1}}(x, y) \quad (5)$$

where  $Z_{\text{LT}^{-1}}(x, y)$  indicates a change in coordinates for the function  $Z(x, y)$ ; that change involves the  $2 \times 2$  matrix  $[\text{LT}^{-1}]$ . Implicitly, this means that  $[\text{LT}]$  is invertible. This assumption is

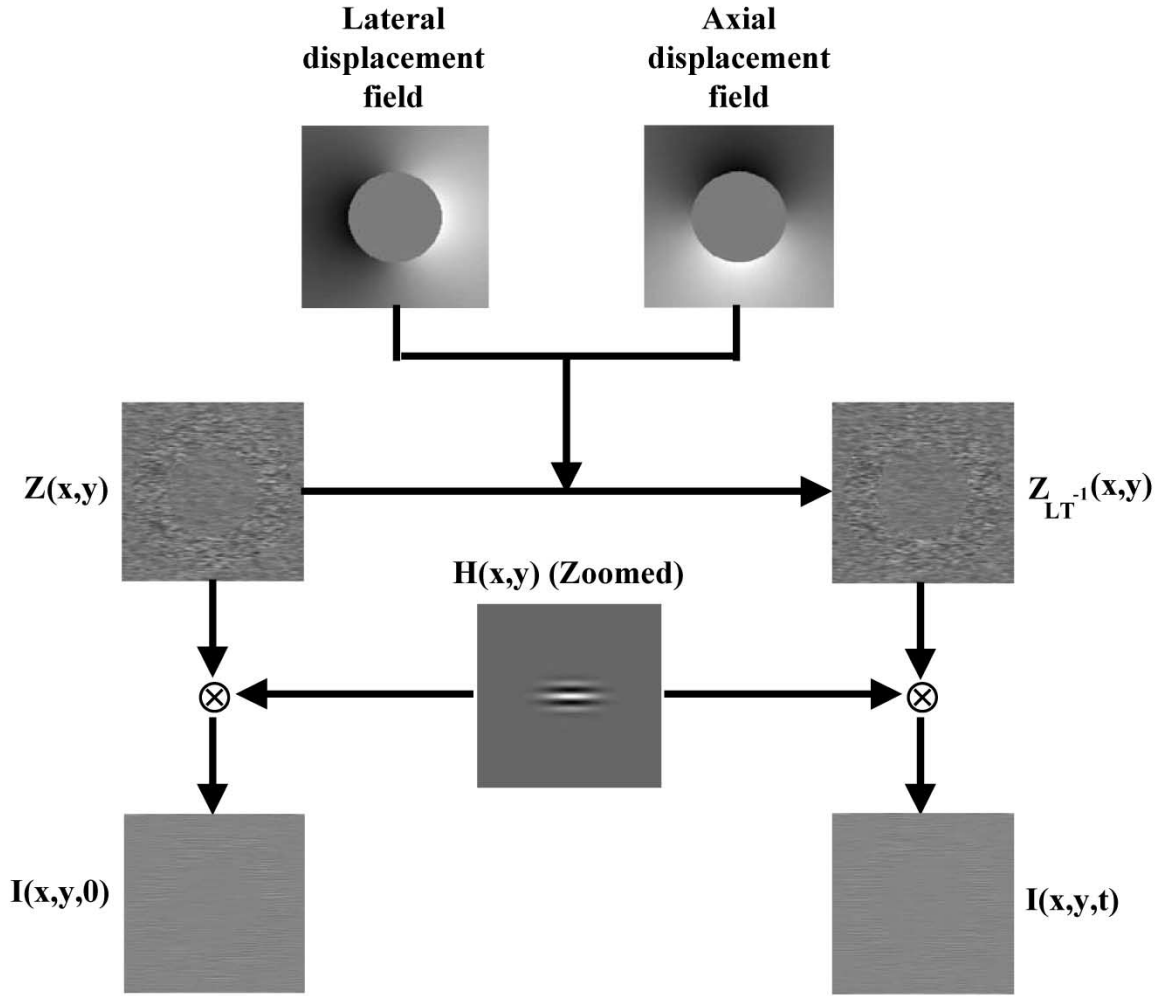


Fig. 2. Schematic implementation of the dynamic image-formation model. For this example, the displacement field was computed from the analytical solution for a pressurized thick-wall cylindrical blood vessel embedded in an elastic coaxial cylindrical medium (Appendix I). The parameters on this figure refer to (5). The dynamic image-formation model was also applied to the case of the heterogeneous vessel. In this case, the displacement field was determined with Ansys simulations.

valid for incompressible continuum. Indeed, in such a case, the determinant of  $[LT]$  (also known as the Jacobian) is unity, so  $[LT]$  is nonsingular and invertible.

1) *Biomechanical Simulation of Tissue Motion:* As a first step, the Matlab software (The MathWorks, Inc., MA, ver. 6.0) was used to simulate the simple case of a homogeneous vessel wall. The process is schematically presented in Fig. 2 and can be summarized as follows. It started by generating in Matlab a scattering function that simulated the acoustical characteristics of a transverse vascular section; that provided  $Z(x,y)$ . The analytical solution for a pressurized thick-wall cylindrical blood vessel embedded in an elastic coaxial cylindrical medium was then derived (Appendix I). From that, the axial and lateral displacement fields were computed. Those displacement fields were applied upon  $Z(x,y)$  to perform motion and then to provide  $Z_{LT}^{-1}(x,y)$ . Finally,  $Z(x,y)$  and  $Z_{LT}^{-1}(x,y)$  were, respectively, convolved with  $H(x,y)$  (the PSF) to produce the pre-tissue-motion and the post-tissue-motion RF images ( $I(x,y,0)$  and  $I(x,y,t)$ ,  $t \neq 0$ ). As it is seen in the next section, those two images constitute the inputs to the LSME.

A pathologic (heterogeneous) vessel wall was also investigated, that is the case where the lumen is narrowed by the presence of a hard plaque at the intima. The process to simulate the pre-tissue-motion and the post-tissue-motion RF images was similar to the homogeneous case study, except that the Ansys finite-element modeling software (Ansys Inc., Canonsburg, PA, ver. 6.0) was used to describe the static mechanical behavior and the kinematics of the pressurized heterogeneous vessel.

### C. The Lagrangian Speckle Model Estimator (LSME)

The Lagrangian speckle estimator was introduced and widely discussed in [16]. It is a model-based estimator that relies on the previous tissue-motion and dynamic image-formation models. It can be formulated as a nonlinear minimization problem. The LSME iteratively computes the  $[LT]$  that allows the best match within a sequence of images; it, thus, provides the strain tensor through (1)–(3). For simplicity and without loss of generality, let us consider only two images of the sequence:  $I(x,y,t)$  at  $t = 0$ , that is  $I(x,y,0) = I_0(x,y)$  which is labeled as the pre-tissue-motion image; and  $I(x,y,t)$  at a given time ( $t_1 \neq 0$ ) such

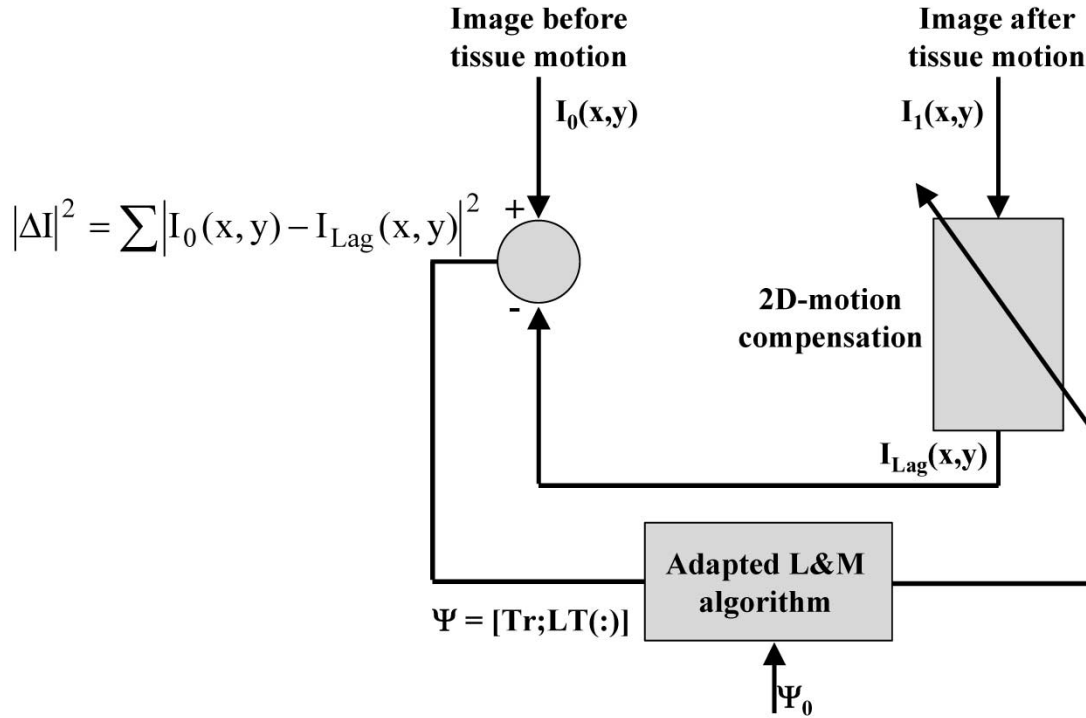


Fig. 3. Block-diagram showing the implementation of the Lagrangian speckle motion model estimator [see (6)]. The algorithm searches the tissue motion vector  $\Psi$  that best matches  $I_0$  and  $I_1$ .  $\Psi_0$  is the initial guess that is required to start the iterative process. In this study, a 2% axial compression was assumed for the initial guess.

that  $I(x, y, t_1) = I_1(x, y)$ , which corresponds to the post-tissue-motion image. The estimator is schematically represented by the block-diagram of Fig. 3 and it can be expressed as

$$\underset{\Psi}{\text{MIN}} |I_0(x, y) - I_{Lag}(x, y)|^2 \quad (6)$$

with  $\Psi = [Tr; LT(:)]^T$ .  $I_{Lag}(x, y)$  is labeled as the Lagrangian speckle image; it can be expressed as  $[I_1(x, y)]_{LT}$ , that is the post-motion RF image  $I_1(x, y)$  compensated for tissue motion. In Fig. 3, this is implemented through an adapted version of the Levenberg-Marquardt (L&M) minimization algorithm [22], [23].

Such an estimator provides many advantages. The major one is related to the fact that it allows computing the full 2-D-strain tensor [see (3)]. As  $\Delta_{xx} (= \varepsilon_{xx})$  and  $\Delta_{yy} (= \varepsilon_{yy})$ , the divergence parameters, provide information about tissue stiffness, the shear parameters,  $\Delta_{xy}$  and  $\Delta_{yx}$ , may provide useful insights on the heterogeneous nature of the tissue under investigation. However, one should be aware that the accuracy of the lateral parameters ( $\Delta_{xx}$  and  $\Delta_{xy}$ ) is potentially limited by the lateral resolution of ultrasound systems (the lateral resolution, that depends on the ultrasound beam characteristics, is generally lower than the axial resolution determined by the transducer bandwidth and the ultrasound system electronic properties).

#### D. The Forward Problem: Tissue Motion Analysis

For a continuum, motion can be described in a Lagrangian coordinate system or in an Eulerian coordinate system [24], [25].

<sup>1</sup>This is the Matlab notation for augmented vector  $(:)$  and matrix vectorization  $(:)$ . Hence,  $\Psi$  is a  $6 \times 1$  vector built from the  $2 \times 1$   $Tr$  vector and the  $4 \times 1$  vectorization of  $LT$ .

In the literature, the Eulerian coordinate system is sometimes referred to as the observer's coordinate system, whereas the Lagrangian coordinate system is known as the material coordinate system. The material coordinates allow to express each portion of the continuum as a function of time and position. The difference between these two coordinate systems is illustrated in Fig. 4, where the  $(x, y)$  constitutes the observer's coordinates and the  $(r, \varphi)$  defines the material coordinates.

With most imaging systems, such as ultrasonography, the observer's and the material coordinate systems are generally the same; hence, most tissue motion estimators use, by definition, the observer's coordinate system. However, the material coordinates were presented in [16] as a suitable way to describe speckle dynamics. It was demonstrated that such a coordinate system leads to appropriate signal processing, which allows to counteract speckle decorrelation effects in tissue motion assessment. In noninvasive vascular elastography, as illustrated in Fig. 1, the observer's coordinate system is the Cartesian  $(x, y)$ -plane. This system is different from the motion coordinate system that is in the radial  $(r, \varphi)$ -plane. In such a situation, the parameters of an estimator are expected to be very difficult to interpret. The challenge of noninvasive vascular elastography greatly concerns the interpretation of the estimated motion parameters to characterize the vascular tissue. In the next sections, such motion parameters are investigated and a proposition is given for a new tissue characterization parameter.

*1) Motion Analysis for a Homogenous Tissue:* To initiate the FP, a pathology-free situation was considered, that is the simplest case of a circular, axis-symmetric and homogeneous vessel

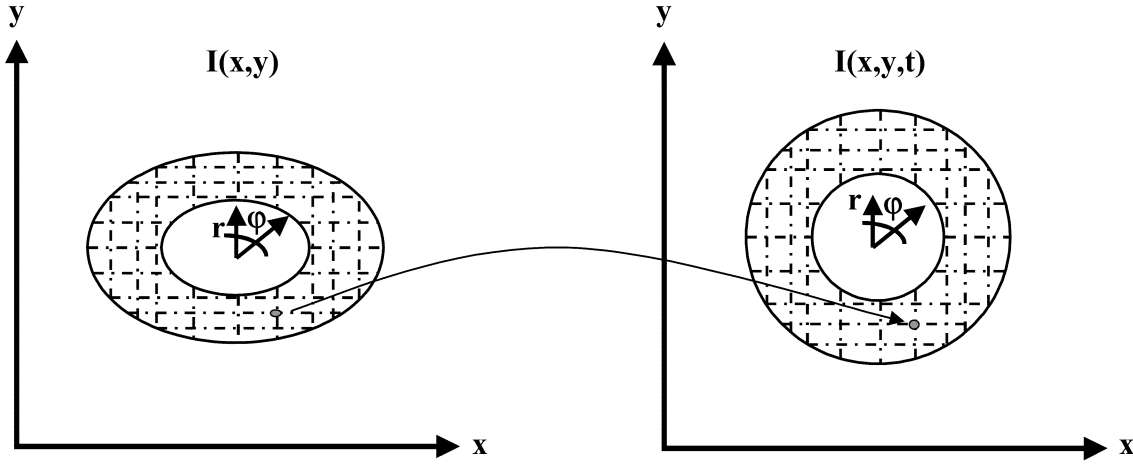


Fig. 4. Illustration of the difference between the observer's  $(x, y)$  and the material  $(r, \varphi)$  coordinate systems. The latter, also known as the Lagrangian coordinate system, considers each portion of a continuum as if it were a particle, for which the trajectory is described as a function of time.

section. To take into account the constraints induced by the environmental tissues and organs, it is hypothesized that the vessel section is embedded in an infinite medium of higher Young's modulus. An exact solution of a pressurized thick-wall cylindrical blood vessel of inner and outer radii  $R_i$  and  $R_o$ , respectively, embedded in an elastic coaxial cylindrical medium of radius  $R_e$ , is derived for our study in linear elasticity. The details are presented in Appendix I. In this paper, it is assumed that the plane strain condition for the vessel wall applies and also that the two media are incompressible and isotropic. Referring to Appendix I, the displacement gradient components [see (2)] are given by

$$\Delta(x, y) = \begin{bmatrix} K_\infty \frac{y^2 - x^2}{(x^2 + y^2)^2} & -2K_\infty \frac{xy}{(x^2 + y^2)^2} \\ -2K_\infty \frac{xy}{(x^2 + y^2)^2} & K_\infty \frac{x^2 - y^2}{(x^2 + y^2)^2} \end{bmatrix} \quad (7)$$

with

$$K_\infty = \frac{3}{2}P_b \left[ E^{(1)} \left( \frac{1}{R_i^2} - \frac{1}{R_o^2} \right) + \frac{E^{(2)}}{R_o^2} \right]^{-1} \quad (8)$$

where  $^{(1)}$  and  $^{(2)}$ , respectively, describe the vessel wall and the external medium;  $P_b$  defines the blood pressure and  $E$  is the Young's modulus.

Using Matlab software, (7) and (8) were processed to simulate the dynamics of a homogeneous vessel section subjected to an intraluminal pressure gradient of 73 mmHg; that is close to 6% intraluminal dilation<sup>2</sup> for the constitutive model presented in Appendix I. The physical vessel dimensions were 7-mm outer diameter and 4-mm inner diameter as to approximate the physiological case of a femoral artery. Fig. 5(a) and (b), respectively, presents the lateral and axial displacement fields. Maximum motion occurred at the lumen. Fig. 5(c)–(f) presents the  $\Delta_{ij}$  components of (7), which are, respectively, the lateral strain, the lateral shear, the axial shear, and the axial strain.

<sup>2</sup>Notice that 6% intraluminal dilation is equivalent to 3% compression of the intraluminal wall.

The elastogram, i.e., the map of the axial strain distribution, is generally presented as a grayscale image. Because in conventional elastography, external y-axis compression is applied and also because 1-D y-axis motion is assessed,  $\Delta_{yy}$  is expected  $\leq 0$ . Traditionally, smaller strain amplitude values are associated with harder regions and are printed in black; equivalently, higher strain amplitude values are associated with softer regions and are printed in white. However, in NIVE, as it can be observed in Fig. 5(f), dilation can also be detected ( $\Delta_{yy} \geq 0$ ) in the elastogram. In an elastographic sense, the dilation regions can be misinterpreted as soft tissue. Indeed, in Fig. 5(f), two harder zones ( $\Delta_{yy} \leq 0$ ) likely seem to be identified at 12 and 6 o'clock. Because, for the conditions simulated, the vessel wall is homogeneous, such a phenomenon is referred to as hardening artefact [26]. Inversely, two softer zones ( $\Delta_{yy} \geq 0$ ) at 3 and 9 o'clock seem also to be identified; they are referred to as softening artefacts. Such motion artefacts stem from the fact that motion occurs radially and is observed in Cartesian coordinates; this can constitute a potential limitation to noninvasive vascular elastography.

To go further with this observation, let us consider the motion parameters in their natural polar coordinate system, or material coordinate system. In Fig. 6(a), is presented the radial displacement field computed from the lateral and axial displacement fields [Fig. 5(a) and (b), respectively]. This radial displacement field is also presented in a polar  $(r, \varphi)$  coordinate system [Fig. 6(b)]. The gradient of the latter displacement field, thus, provides the radial strain [Fig. 6(c)]. Fig. 6(d) shows a plot of the radial strain at  $\varphi = \pi$ . One can observe the monotonic profile of this plot, being maximal at the lumen and minimal at the outer side of the vessel; such a phenomenon is a consequence of the boundary conditions and is known in the literature as the strain decay [8]. Finally, in Fig. 6(e), the radial strain is reported back in the  $(x, y)$  coordinate system. Regardless of the strain decay phenomenon, one can observe that no

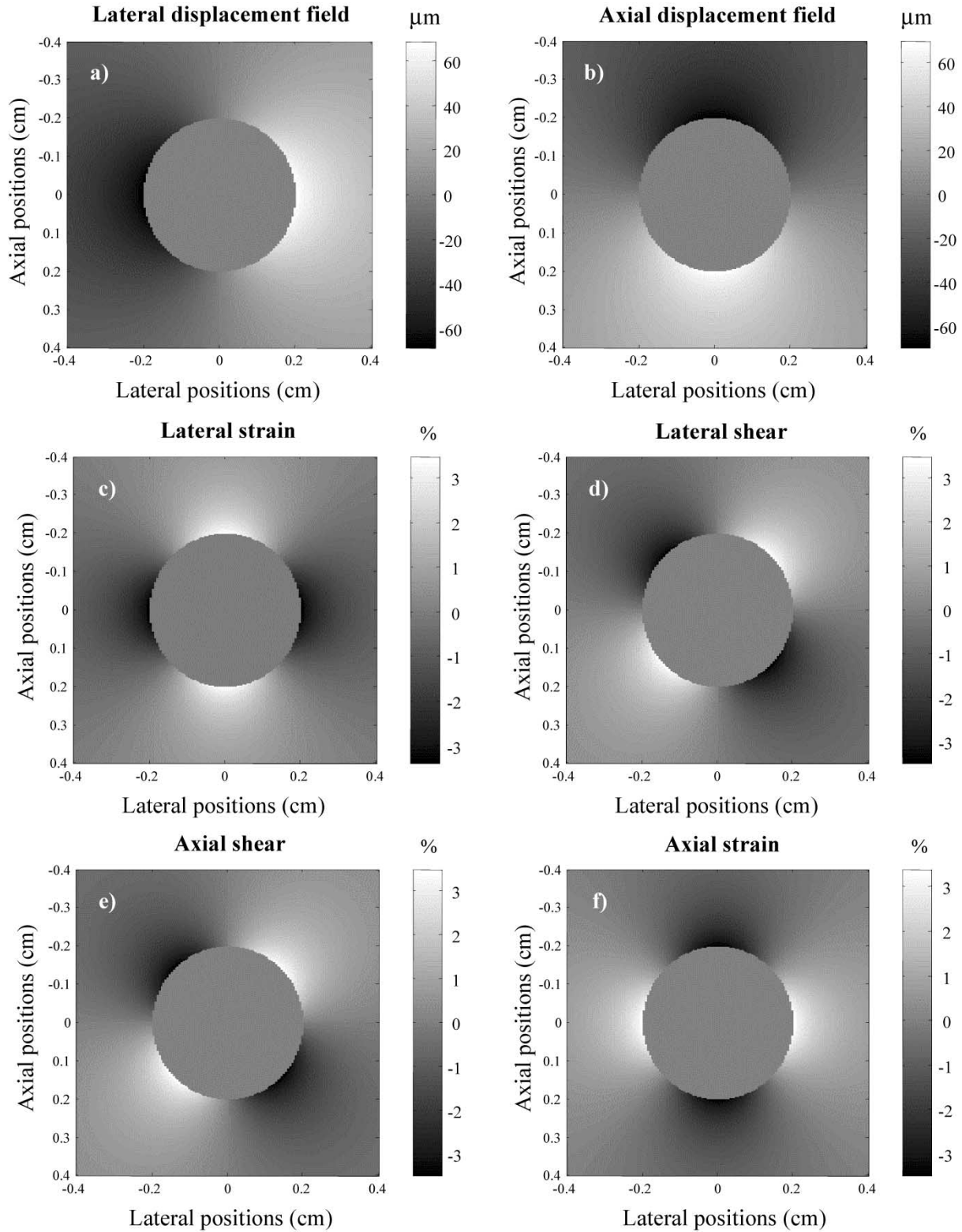


Fig. 5. Motion parameters for a pressurized thick-wall cylindrical blood vessel, embedded in an elastic infinite medium. (a) and (b) Lateral and axial displacement fields, respectively; the colorbars express the displacements in micrometers. (c)–(f) The  $\Delta_{ij}$  components of (3) which are, respectively, the lateral strain ( $\Delta_{xx}$ ), the lateral shear ( $\Delta_{xy}$ ), the axial shear ( $\Delta_{yx}$ ), and the axial strain ( $\Delta_{yy}$ ); the colorbars express the strain in percent.

specific hard or soft region is identified. Fig. 6(e), thus, illustrates a strain profile that is quite representative of a homogeneous vessel wall behavior.

2) *A New Parameter for Tissue Characterization*: Hopefully, elastograms such as the one in Fig. 6(e) are required to appropriately characterize the vessel wall. However, to prevent signal

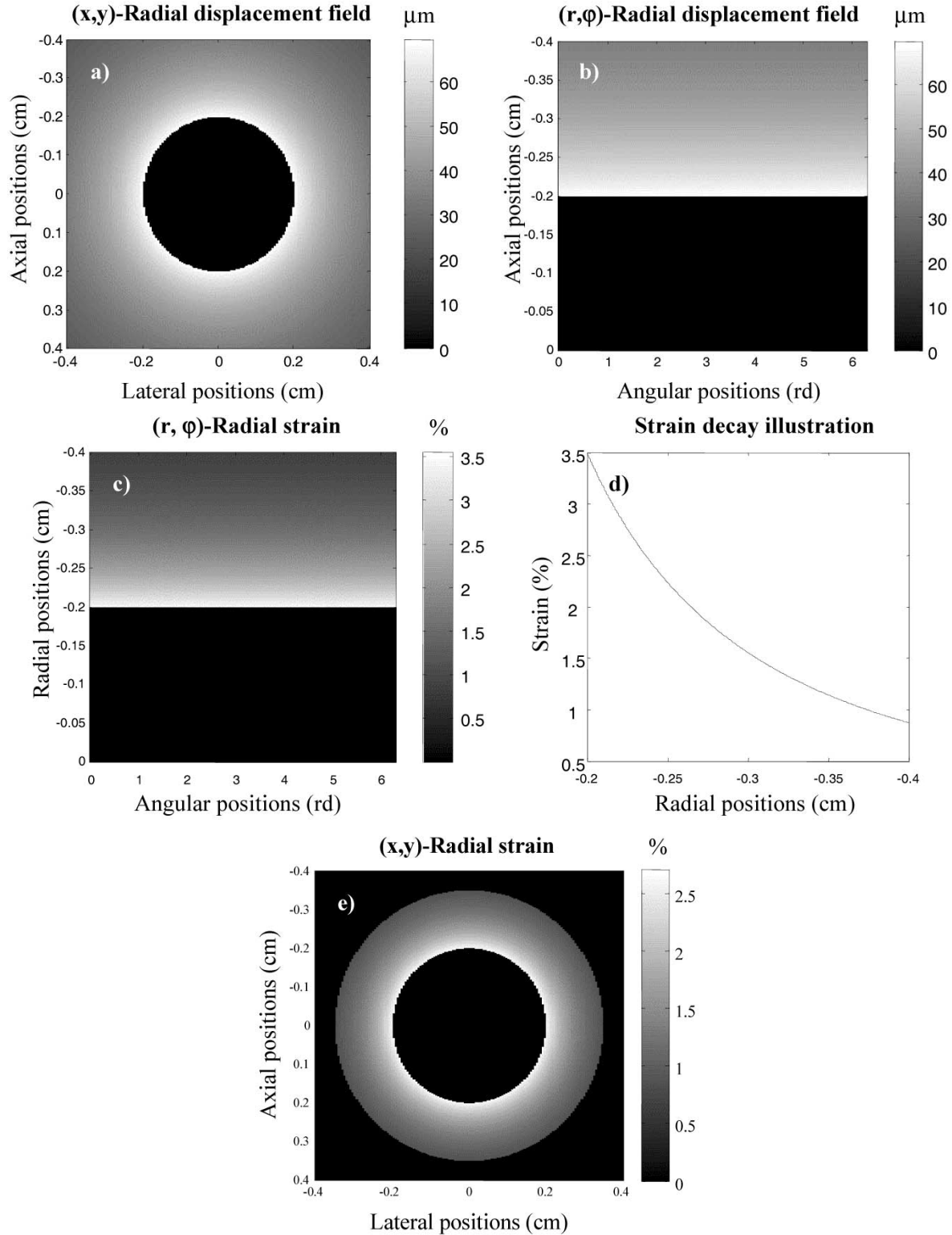


Fig. 6. Radial strain and strain decay for a homogeneous vessel wall. (a) Radial displacement computed from the lateral and axial displacement fields; (b) radial displacement field in a polar  $(r, \varphi)$  coordinate system; (c) radial strain computed from the gradient of (b); (d) radial strain at  $\varphi = \pi$  showing the strain decay; (e) radial strain reported back in the  $(x, y)$ -coordinate system.

decorrelation in NIVE, motion is to be studied in the transducer coordinate system; that is the  $(x, y)$ -Cartesian coordinates. Accordingly, elastograms are expected to be as artefactual as the one in Fig. 5(f). However, taking a close look at all the motion

parameters in Fig. 5, one can observe that  $\Delta_{xx}$  and  $\Delta_{yy}$  are complementary, while  $\Delta_{xy} = \Delta_{yx}$ . In this paper, the VM coefficient is proposed as a parameter to characterize the vessel wall [27], [28]. Indeed, VM is independent of the coordinate system and



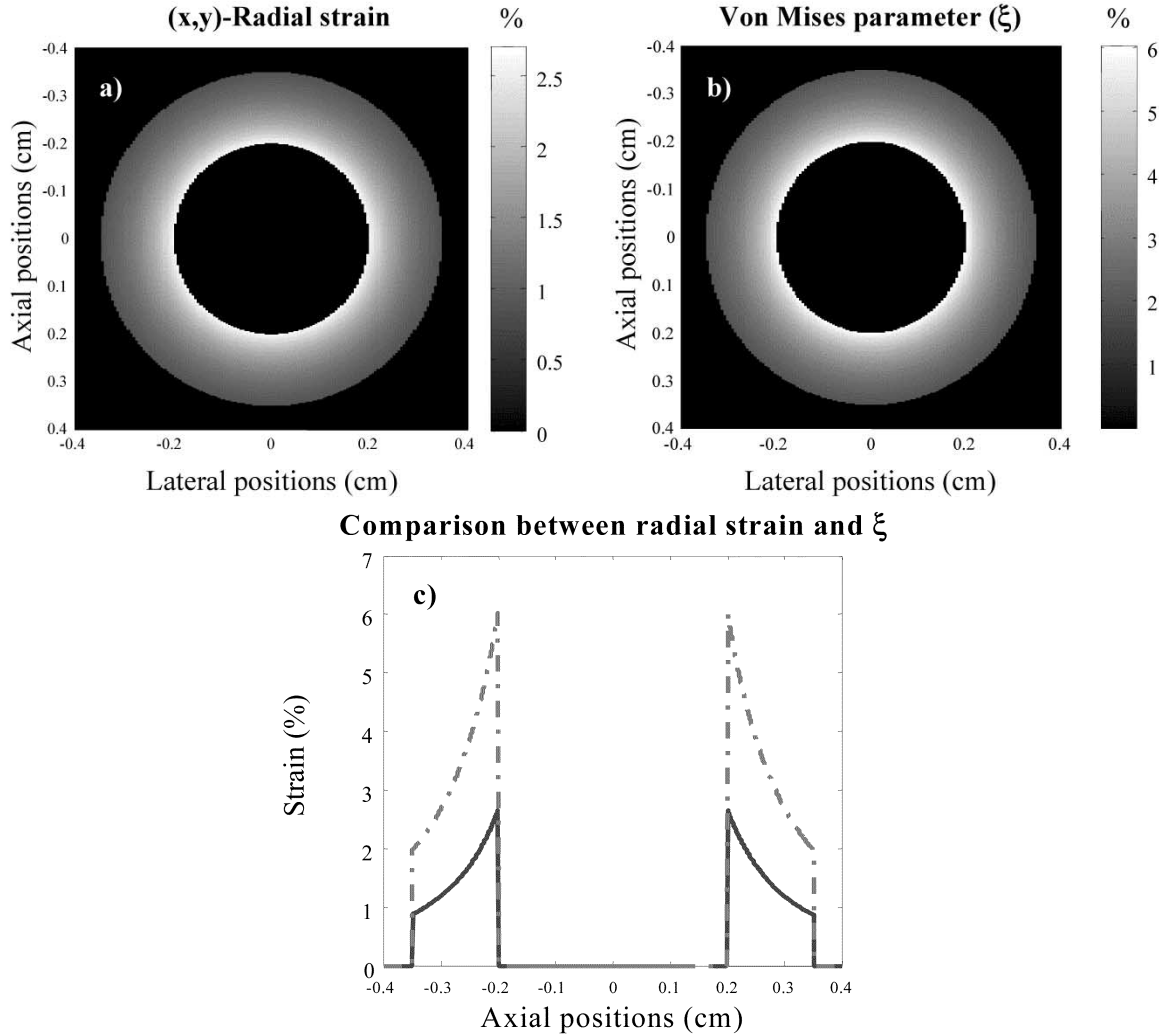


Fig. 7. Comparison between the radial strain and the VM parameter ( $\xi$ ) for a homogeneous vessel wall. (a) Radial strain in the  $(x, y)$ -coordinate system. (b) Map of  $\xi$ ; (c) curves from the radial strain (—) and  $\xi$  (---) at  $x = 0$ .

is a combination of the four displacement gradient components ( $\Delta_{ij}$ ) that is mathematically expressed as

$$\begin{aligned} \xi &= \sqrt{\varepsilon_{xx}^2 + \varepsilon_{yy}^2 - \varepsilon_{xx}\varepsilon_{yy} + 3\varepsilon_{xy}^2} \\ &= \sqrt{\Delta_{xx}^2 + \Delta_{yy}^2 - \Delta_{xx}\Delta_{yy} + \frac{3}{4}(\Delta_{xy} + \Delta_{yx})^2}. \end{aligned} \quad (9)$$

In Fig. 7, a comparison between  $\xi$  and the radial strain [Fig. 6(e)] is presented. Qualitatively, both parameters are equivalent. Fig. 7(c) shows the plots for the radial strain (—) and  $\xi$  (---) at  $x = 0$ . Analyzing those curves, one can observe that the VM coefficient likely improves the contrast between higher and lower strains while the profile remains the same. Moreover, regardless of the strain decay,  $\xi$  (as well as the radial strain) is interestingly free of hardening or softening artefacts. It is, thus, allowed believing that such a parameter could be very suitable to noninvasively characterize the vessel wall. To corroborate such an assumption, a more complex geometry, that is a heterogeneous vessel wall, is considered in the next section.

3) *Characterization of an Heterogeneous Vessel Wall:* The case of a pathologic vessel wall is now investigated, that is when

the lumen is narrowed by the presence of a hard plaque at the intima. It is assumed that the plaque is ten times stiffer than the normal vascular tissue, a lipid pool ten times softer than the normal vascular tissue immediately surrounds it. The geometry is schematically presented in Fig. 8(a). To have approximately the same range of strains as in the homogenous case study, the intraluminal pressure gradient was set at 40 mmHg (intraluminal dilation close to 6%). The outer diameter of the vessel was again set at 7 mm. In Fig. 8(b)–(e), the four  $\Delta_{ij}$  tensor components are presented. One can appreciate the very complex patterns of those parameters. The elastogram (i.e., the axial strain map), presented in Fig. 8(e) (equivalently the lateral strain map of Fig. 8(b), shows a region of relatively high strain values; this corresponds to the location of the lipid pool as it can be expected. Nevertheless, the elastogram does not undoubtedly allow differentiating between the plaque, the lipid pool and the normal vascular tissue.

In Fig. 9(b), the *elastogram* computed using the VM parameter ( $\xi$ ) is presented. Obviously, three main regions are identified: the hard plaque with lower strain values, the lipid pool with higher strain values and the normal tissue with moderate strain values. This elastogram can qualitatively be compared with the

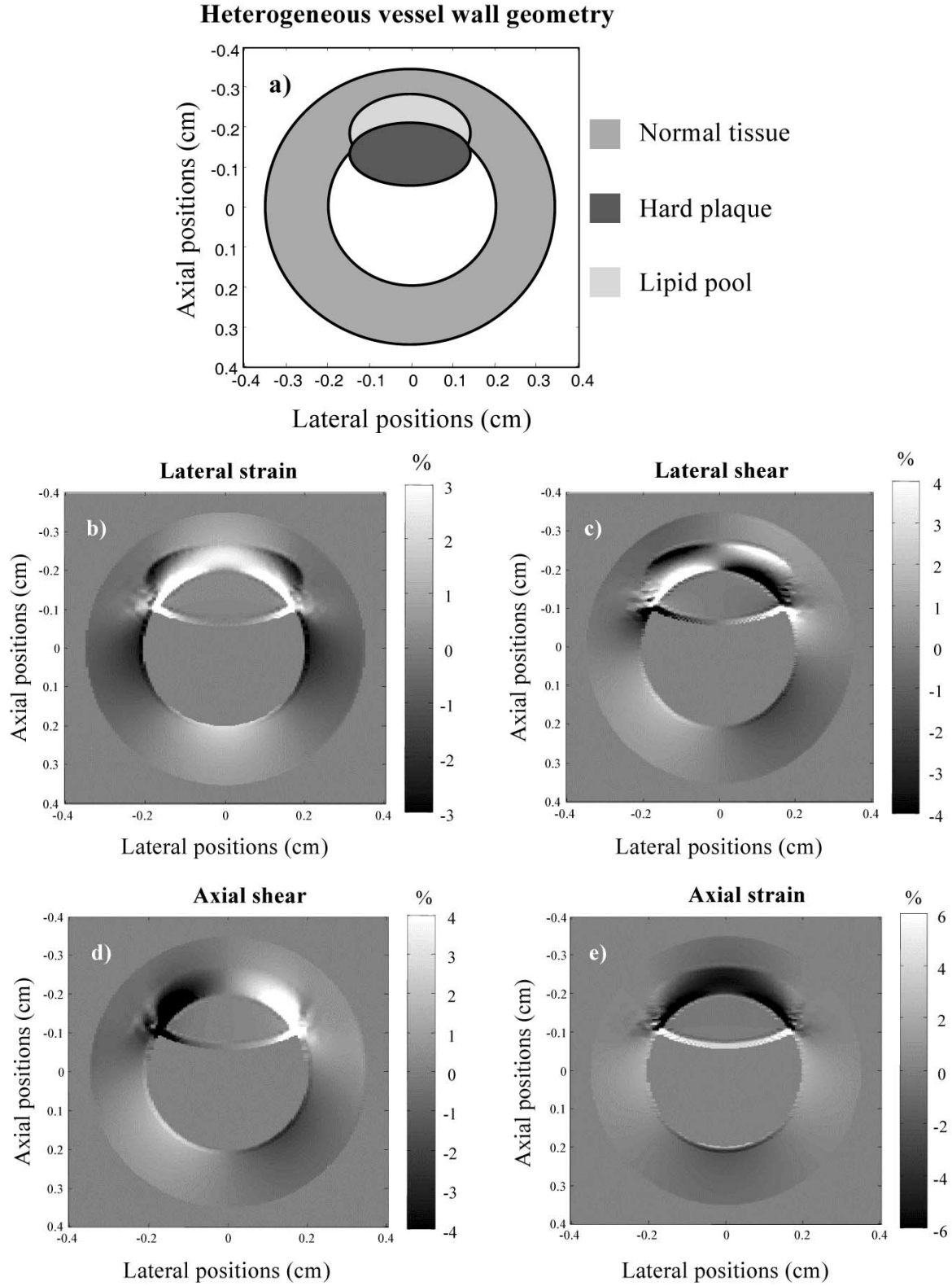


Fig. 8. Motion parameters for an heterogeneous vessel wall. (a) Simplified representation of the geometry; (b)–(e) shows the  $\Delta_{ij}$  components of (3), which are, respectively, the lateral strain ( $\Delta_{xx}$ ), the lateral shear ( $\Delta_{xy}$ ), the axial shear ( $\Delta_{yx}$ ), and the axial strain ( $\Delta_{yy}$ ); they were computed from the gradients of the lateral and axial displacement fields. The colorbars express the strain in percent.

radial strain map presented in Fig. 9(a). For a quantitative comparison, Fig. 9(c) shows plots of the radial strain and  $\xi$  at  $x = 0$ . In both of them, the three specific regions can be clearly dif-

ferentiated. As it was also observed in the homogeneous case study, it is interesting to point out that  $\xi$  substantially improves the contrast between soft and hard tissues.

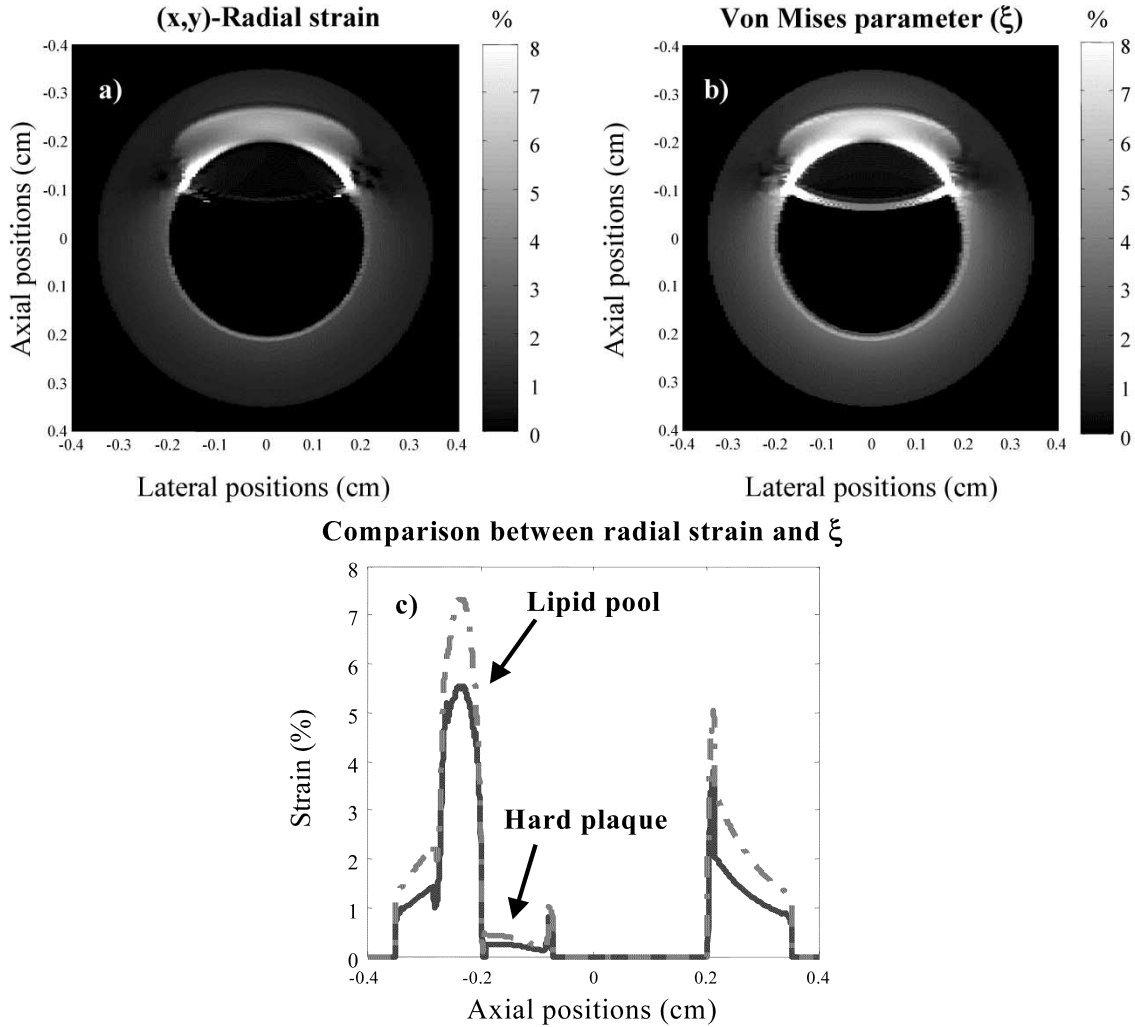


Fig. 9. Comparison between the radial strain and the VM parameter ( $\xi$ ). (a) Map of the  $(x, y)$ -radial strain; (b) map of  $\xi$ ; (c) curves of a (—) and b (---) at  $x = 0$ .

These observations are interesting and allow believing in the potential application of NIVE. Nevertheless, some artefacts still remain, specifically at the intersections between hard, soft, and normal tissues. This is, unfortunately, quite expectable since those are sites of maximal stress concentrations. Such a problem could have been circumvented if the Young's modulus, instead of a strain parameter, was computed in ultrasound elastography. Another problem, which could arise in the real-life situation, concerns the limited lateral resolution of current ultrasound systems. Because of that, variances in the lateral motion estimates ( $\Delta_{xx}$  and  $\Delta_{xy}$ ) may in practice be large. This may constitute a potential limitation to the assessment of  $\xi$ . In the next sections, we present results from simulated RF data. All elastograms were computed with the LSME.

### III. RESULTS

#### A. Application of the LSME to Simulated RF Echo Signals

The dynamic image-formation model of (5) was used to simulate sequences of RF images. As illustrated in Fig. 2, the vessel section [the scattering function  $Z(x, y)$ ] was modeled as a 2-D white Gaussian noise

(number of scatters in a resolution cell  $\gg 5$ ). The lumen and the tissue surrounding the vessel were assumed to be, respectively, 2.5 and 1.67 times less echoic than the wall.  $Z(x, y)$  was low-pass filtered before considering motion; the post-motion scattering function was expressed as  $Z_{LT-1}(x, y)$ . The radial displacement field used to mimic motion was obtained from the analytical biomechanical model presented in Appendix I (normal cylindrical vessel), and Ansys simulations (obstructed vessel with a plaque). It is important to remember that such a motion is normally induced by the cardiac pulsation. The imaging system PSF ( $H(x, y)$ ) was defined as a 2-D Gaussian wavelet, modeling a 10-MHz transducer with a 60% bandwidth at  $-3$  dB and a beamwidth (width at half maximum) of 0.6 mm. The simulated RF images (pre-tissue-motion and post-tissue motion images) were used as inputs by the LSME to compute the four displacement gradient components. Are presented, in the next two sections, results for the homogenous and the heterogeneous vessel wall studies, respectively.

1) *Motion Estimation for a Homogenous Vessel Wall:* As defined in Section II-D1, a vessel of 7-mm outer diameter and 4-mm inner diameter was simulated. To take into account the surrounding tissue, the echo field was 8 mm  $\times$  8 mm; that is

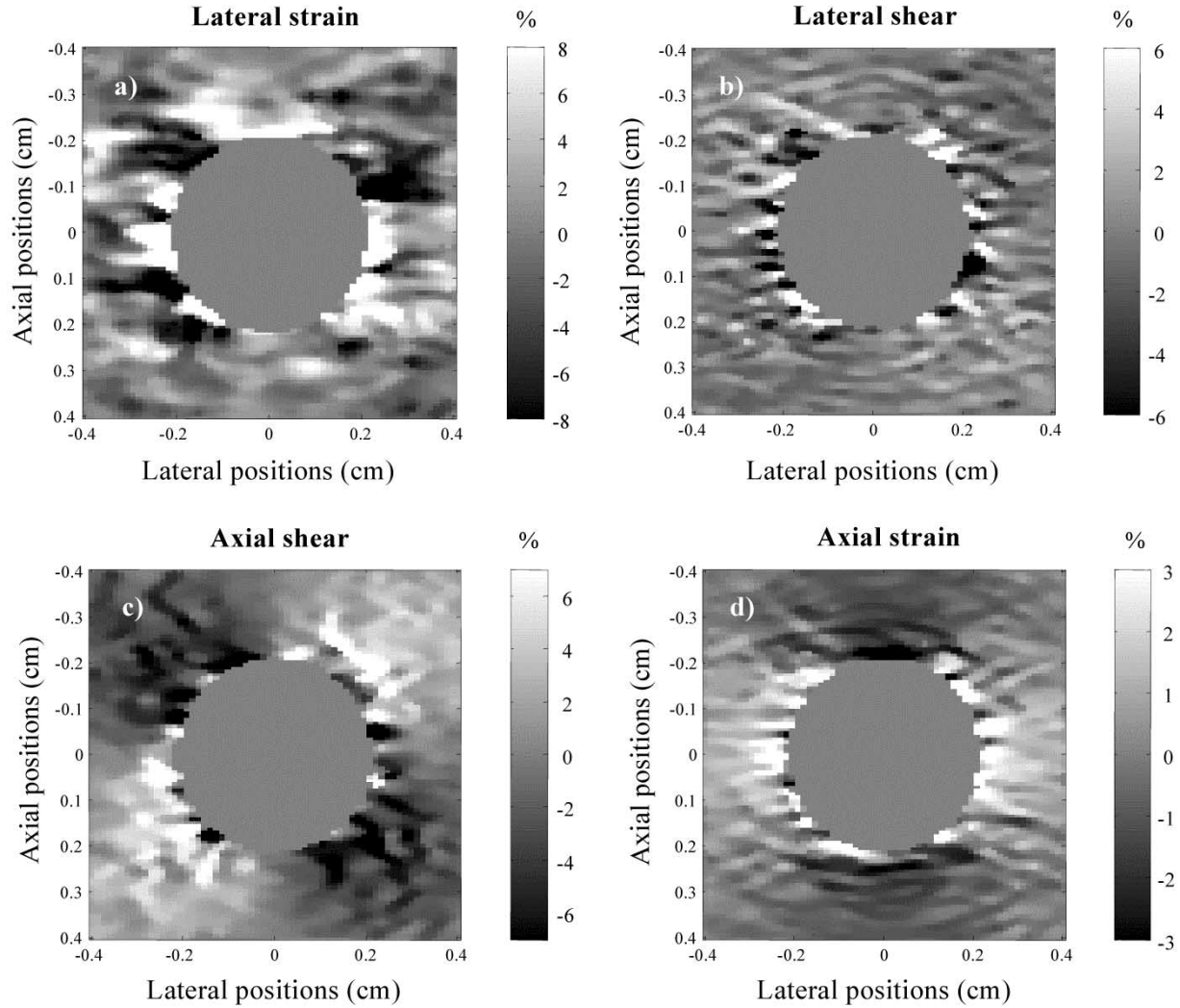


Fig. 10. Motion parameters as computed with the LSME for a homogenous vessel wall; (a)–(d)  $\Delta_{ij}$  components of (3), which are, respectively, the lateral strain ( $\Delta_{xx}$ ), the lateral shear ( $\Delta_{xy}$ ), the axial shear ( $\Delta_{yx}$ ), and the axial strain ( $\Delta_{yy}$ ).

3000 samples axially  $\times$  150 RF lines laterally. To apply the LSME, a measurement-window of  $533 \mu\text{m} \times 1\,066 \mu\text{m}$  (200 samples  $\times$  20 RF lines) was chosen. As illustrated in Fig. 1, the motion was estimated for windows  $W_{\text{mm}}$  with 88% and 90% axial and lateral overlap, respectively.

The windowed data of the pre and post-tissue-motion images were preprocessed to compensate for tissue translation using 2-D correlation. This left the LT matrix and eventually a small residual translation motion ( $\theta_1$  and  $\theta_4$ ) to estimate. In this paper, the translation motion parameters  $\theta_1$  and  $\theta_4$  were not considered. The four displacement gradient components, as computed with the LSME, are presented in Fig. 10(a)–(d).

Fig. 10(a) and (b) presents the maps of the lateral strain and shear, respectively. As it can be expected, those motion parameters show large variances. That is due to the limited lateral image resolution ( $53 \mu\text{m}$  per RF line, for this study) used to simulate the performance of current ultrasound systems. Nevertheless, the lateral strain values are observed in a range, on average,

that includes the theoretical results [Fig. 5(c)]. Fig. 10(c) and (d) presents maps of the axial shear and strain, respectively. The elastogram [Fig. 10(d)] is quantitatively similar to the theoretical one [Fig. 5(f)], showing strains in the interval of  $[-3\%, 3\%]$ . The pattern of the axial shear is also quantitatively similar to the theoretical one [Fig. 5(e)].

Fig. 11 presents comparisons between the simulated and theoretical VM parameters  $\xi$ . For a quantitative comparison, Fig. 11(b) presents an average of three curves around  $x = 0$ , and at Fig. 11(d) the curve corresponds to  $x = 0$ . Notice the presence of strain decay in each curve. It is also important to emphasize that close to the lumen, motion estimates may be, in some instances, inaccurate. That is explained by the fact that in such locations, the measurement-windows may overlap the vessel wall (where pre-tissue-motion and post-tissue-motion signals are expected to be coherent) and the lumen (where pre-tissue-motion and post-tissue-motion signals are expected to be uncorrelated). As a consequence of that, such motion

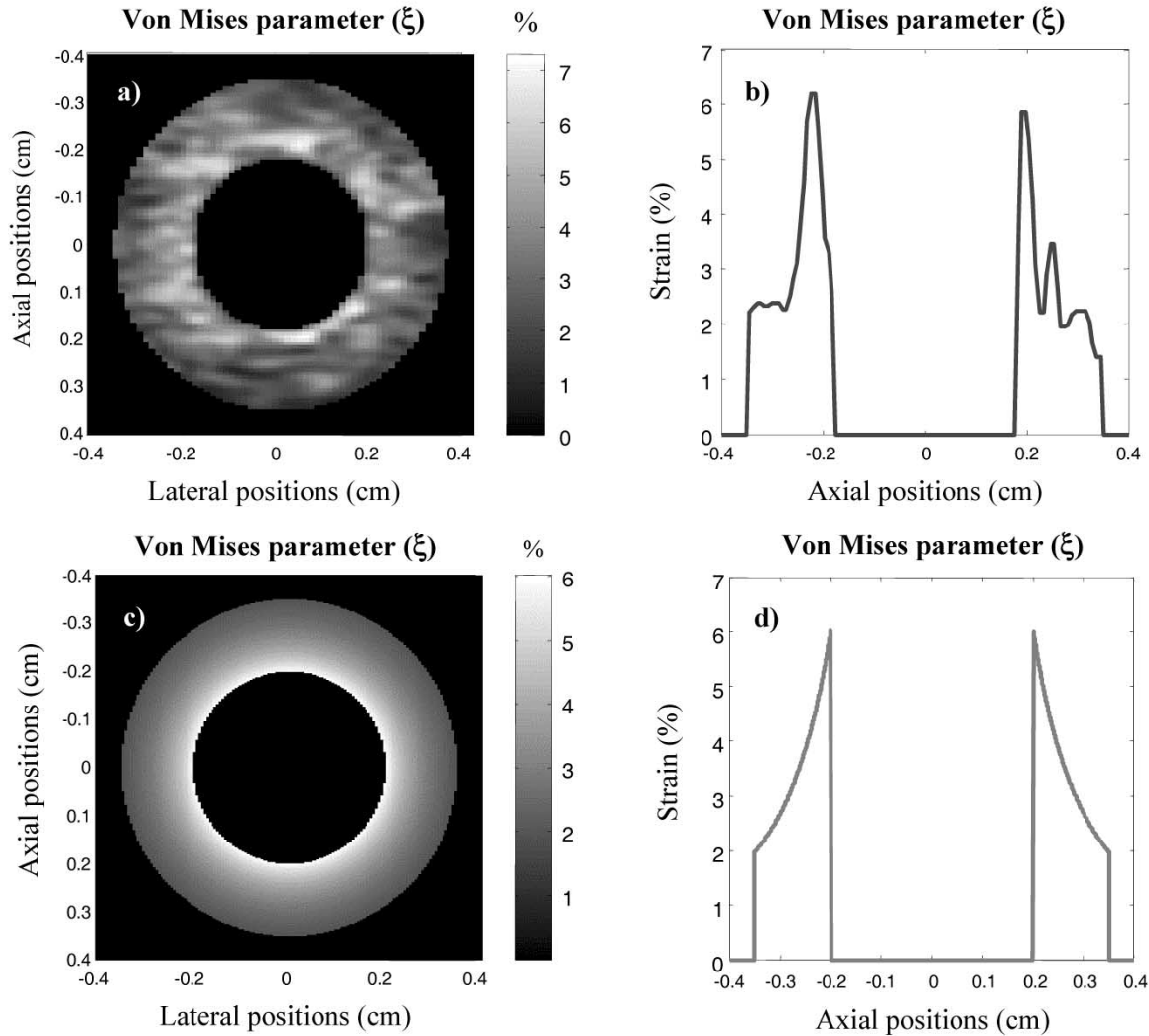


Fig. 11. Comparison between simulated and theoretical VM parameters ( $\xi$ ) for a homogeneous vessel wall. (a) Map of the simulated  $\xi$ . (b) Curve of the simulated  $\xi$  at  $x = 0$ . (c) Map of the theoretical  $\xi$ . (d) Curve of the theoretical  $\xi$  at  $x = 0$ .

estimates may not be reliable. Because one is now aware of some of the eventual difficulties that could be encountered and, in the light of the promising results of Fig. 11, it allows believing in the potential of NIVE. In the next section, the heterogeneous vessel wall is investigated.

2) *Motion Estimation for a Heterogeneous Vessel Wall:* The vessel wall investigated is the same as in Section II-D3. The data acquisition system (i.e., the PSF) and the parameters for motion assessment ( $W_{\text{mm}}$ , overlap, etc.) are the same as in the Section III-A1 above. In Fig. 12, the results for the four displacement gradient components are presented. Fig. 12(a) and (b) presents the maps for the lateral strain and shear, respectively. As for the homogenous case, the variances for those motion estimates are large; they do not clearly allow differentiating between hard and soft structures. Nevertheless, a reasonable range of strain values is, on average, observed when comparisons are made with Fig. 8. The simulated elastogram [Fig. 12(d)] shows a slight underestimation of the axial strain values when compared to the theoretical one [Fig. 8(e)]; strain values in the interval of  $[-2.5\%, 2.5\%]$  are observed instead of  $[-6\%, 6\%]$ . That is, at least partially, due to the fact that high strain areas

at the intersections between hard, soft, and normal tissues are more prominent in the theoretical elastogram than in the simulated one. The axial shear is also qualitatively and quantitatively similar to the theoretical one [Fig. 8(d)]. In Fig. 13(a), is shown the composite elastogram ( $\xi$ ). Even with the presence of large variances on the estimates of the lateral motion parameters,  $\xi$  allows identifying the hard plaque and the soft lipid pool. For a quantitative validation, Fig. 13(b) shows an average of three curves around  $x = 0$ . Clearly the hard plaque (strain values less than 1%) and the lipid pool (strain values around 4%) are detected. Because of the strain decay phenomenon, the normal tissue presents strain values standing from 1% up to 2%. For comparison purpose, the same results are shown for the theoretical  $\xi$  in Fig. 13(c) and (d).

#### IV. DISCUSSION

The vascular tissue is made of elastin, collagen and smooth muscle cells; its mechanical properties are, thus, very complex. Pathological conditions of such a tissue often induce changes in the vessel wall elasticity. For example, plaque deposit stiffens

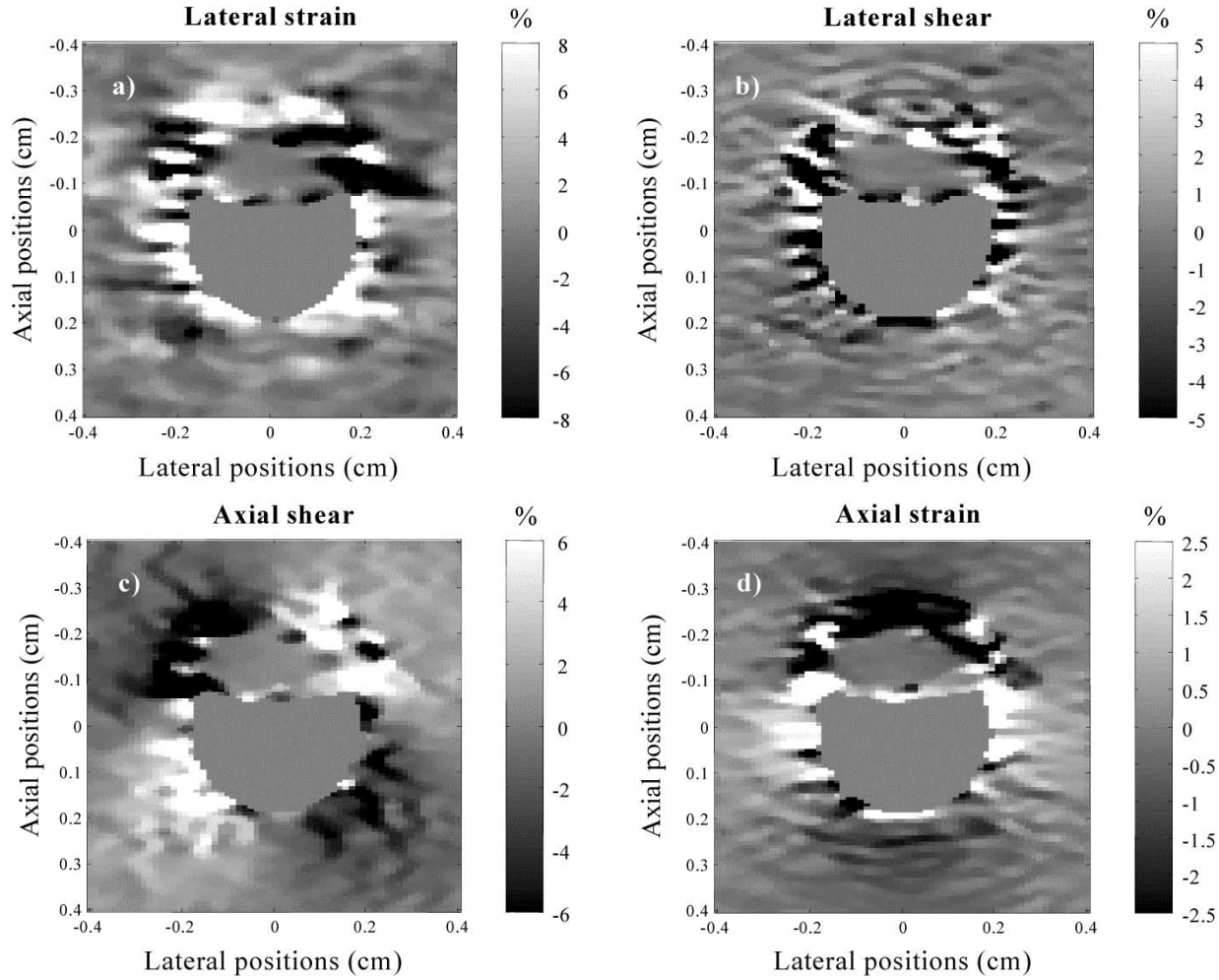


Fig. 12. Motion parameters as estimated with the LSME for an heterogeneous vessel wall; (a)–(d)  $\Delta_{ij}$  components of (3), which are, respectively, the lateral strain ( $\Delta_{xx}$ ), the lateral shear ( $\Delta_{xy}$ ), the axial shear ( $\Delta_{yx}$ ), and the axial strain ( $\Delta_{yy}$ ).

the vascular wall and then counteracts its dilation under systolic blood pressure. On the other hand, peripheral aneurysmal rupture of the aorta has been linked to changes in the proportion and integrity of collagen and elastin. Because of that, vessel diameters as well as their variations during the cardiac cycle were considered as indices to characterize vessel pathologies [29]–[33]. Hence, from a biomechanical perspective, it can be understood that to better appreciate the dynamics of the arterial wall and its pathologies, a more detailed description of the mechanical and elastic properties of the arteries is required.

Elasticity is a very suitable parameter to describe vessel wall function. It may be quantified with compliance, a measurement that expresses the relative change in vessel cross-sectional area as a function of time [33]–[35]. However, a more complete method to outline the elastic properties of the vessel wall seems to be the elastography; indeed, such a technology aims to provide images of the elastic properties of biological soft tissues.

This paper investigated the feasibility of NIVE. It was shown that a major difficulty with this approach stems from the fact that motion occurs radially within the vessel wall while the ultrasound beam propagates axially (linear array transducers

were considered in the present study). Regarding that, a 2-D tissue-motion estimator was required. Moreover, in such a situation, the motion parameters are expected to be very difficult to interpret. One major challenge with NIVE then concerns the interpretation of the motion estimates to appropriately characterize the vascular tissue.

#### A. About the Forward Problem (FP)

As a first step, the FP in NIVE was addressed. Biomechanical simulations of the vascular wall properties were performed and motion parameters were investigated. The FP allowed to better understanding vascular tissue dynamics in NIVE. Indeed, the analytical solution for a homogeneous vascular section subjected to an intraluminal pressure was derived. Ansys simulations were also performed to address the more complex situation of a heterogeneous plaque. Because tissue motion occurs radially within the vessel wall while the motion is assessed in  $(x, y)$ -Cartesian coordinates, the elastogram ( $\Delta_{yy}$ ) was shown to be subjected to hardening and softening artefacts.

To overcome the problems related to those mechanical artefacts, a new characterization parameter ( $\xi$ ) was proposed. Such

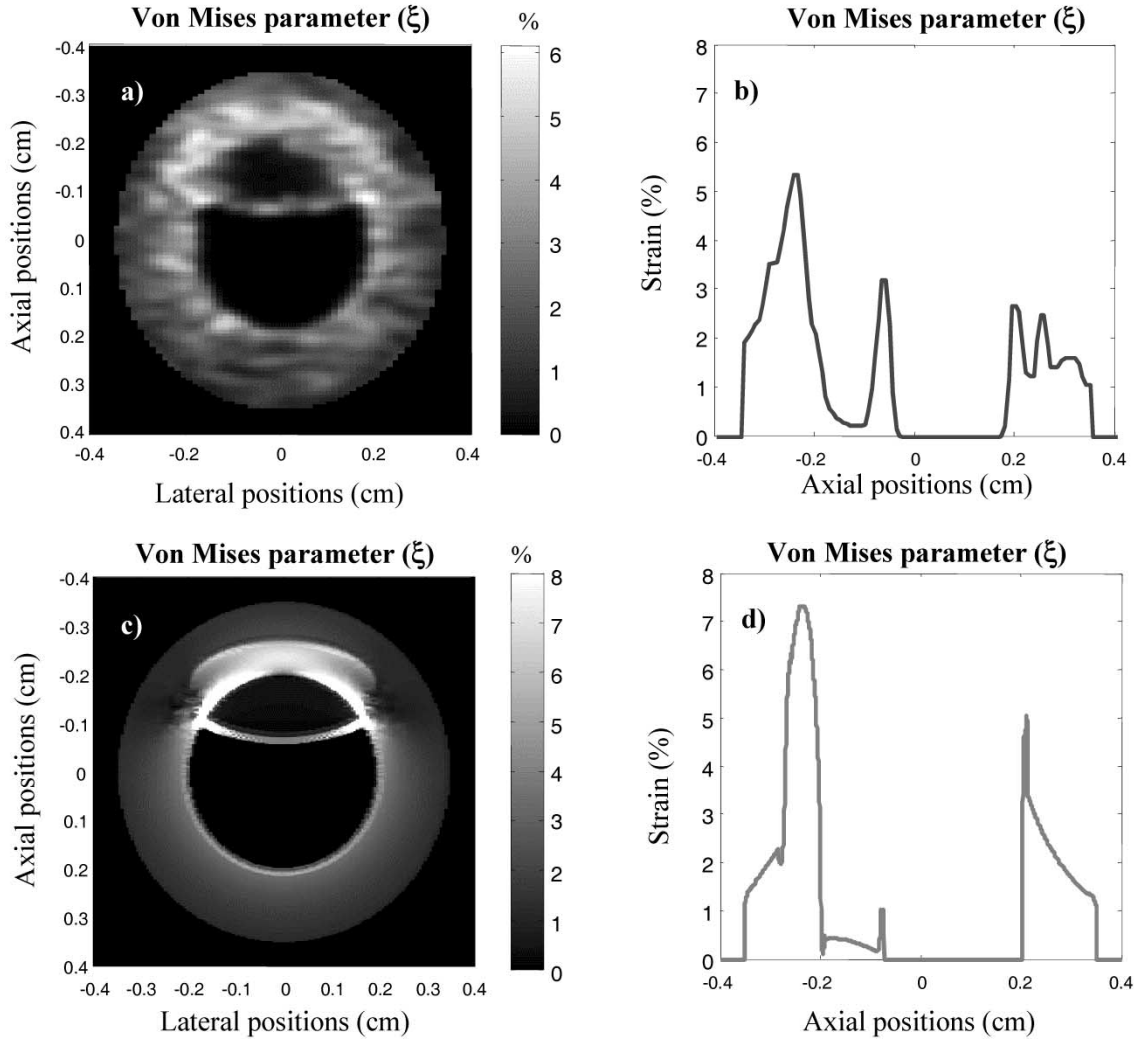


Fig. 13. Comparison between simulated and theoretical VM parameters ( $\xi$ ) for an heterogeneous vessel wall. (a) Map of the simulated  $\xi$ . (b) Curve of the simulated  $\xi$  at  $x = 0$ . (c) Map of the theoretical  $\xi$ . (d) Curve of the theoretical  $\xi$  at  $x = 0$ .

a parameter, also known in the literature as the VM coefficient, uses the full 2-D-strain tensor to provide a measure free from hardening and softening artefacts.  $\xi$  likely allows characterizing the vessel wall in its natural coordinate system. Indeed, such an elastogram presents some similarities with the radial strain map, and even shows up the very well known strain decay as it should be expected. For the case of the simulated pathological vessel, the VM parameter successfully allowed differentiating between hard, soft, and normal vascular tissues. NIVE should then be considered, in some instances, as a promising tool for noninvasively investigating vessel walls.

#### B. About the Application of the LSME

A 2-D-tissue motion estimator, known in the literature as the Lagrangian speckle estimator (LSME), was used to assess motion. The LSME is a 2-D model-based estimator that allows computing the full 2-D-strain tensor. The approach relies on a tissue-motion model and on a dynamic image-formation model. It assumes that the image formation can be modeled as a linear space-invariant operation on a scattering function. Indeed, the

simulated RF images result from the 2-D-convolution operation between the point-spread function of an ultrasound system and the acoustic impedance functions, which were modeled as a white Gaussian noise.

The same data sets as for the FP were investigated. As well, for the homogeneous and heterogeneous vessels, the results seemed promising. The VM characterization parameter ( $\xi$ ) showed great potential to differentiate hard and soft tissues from the normal vascular one. However, the main problem with the LSME remains the assessment of the lateral motion parameters. As a matter of fact, due to the relatively poor lateral resolution of RF images, the variance for those motion estimates is large. It is also important to emphasize that the 2-D motion estimator, presented in this paper, assumes that motion occurs in plane strain condition. However, in practice, because of blood pressure excitation, the vessel wall is also expected to be under distension stress. As a consequence to that, out-of-plane motion will occur in the dynamics between the pre-tissue-motion and the post-tissue-motion RF images; this is another factor that may increase the variance of motion estimates. To at least partially counteract out-of-plane motion,

one could ensure that a small intraluminal pressure gradient is induced. This could be done using an electrocardiogram gating along with the ultrasound acquisition system. The “Lagrangian” filter [16] was also shown to be effective to compensate for such a source of decorrelation noise.

Another potential issue to vascular elastography is that vessel walls are subjected to residual stresses. Indeed, it was demonstrated that the magnitudes of such residual stresses (equivalently residual strains) may be relatively significant [36], [37]. Accordingly, vascular elastograms are expected to be fully valid whenever residual strains are much smaller than strains as induced by the intraluminal pressure gradient. Provided that, in NIVE, elastograms compute maps of relative stiffness, and provided that tissue motion is assessed over small ROIs where linearity is assumed, residual stresses may not have significant effects. Furthermore, another potential solution may consist in setting an optimal pressure gradient such as the tissue strains are much larger than potential residual strains, but are small enough to be in the limits of linear elasticity.

## V. CONCLUSION

An approach to noninvasively characterize vessel walls, labeled as NIVE, has been introduced. Whereas EVE is invasive and its clinical application restricted to a complementary tool to assist IVUS echograms in preoperative lesion assessments and to plan endovascular therapy, NIVE method may be of value to investigate vascular tissue properties of patients under medication, and for post-surgical follow-up. In addition, NIVE could be of interest to investigate small vessels where catheterization and IVUS echography is not possible. While the use of a balloon catheter is not required in NIVE, such an option can be useful if a more precise dilation increment is needed. In this case, however, the technique would be invasive. Regarding the FP, the VM coefficient has been proposed as a new characterization parameter. Numerical simulations showed the potential of the VM parameter to differentiate between hard, soft, and normal vascular tissues. The lateral resolution of current ultrasound systems is, however, a limitation to such an approach.

## APPENDIX

### THICK-WALL CYLINDRICAL BLOOD VESSEL EMBEDDED IN A FINITE (OR INFINITE) MEDIUM

An exact solution of a pressurized thick-wall cylindrical blood vessel of inner and outer radii  $R_i$  and  $R_o$ , respectively, embedded in an elastic coaxial cylindrical medium of radius  $R_e$ , can be found in linear elasticity. For the mathematical formulation, the cylindrical and Cartesian unit base vectors and their associated physical coordinates are noted  $(\vec{e}_r, \vec{e}_\varphi, \vec{e}_z)$ ,  $(\vec{e}_x, \vec{e}_y, \vec{e}_z)$  and  $(r, \varphi, z)$ ,  $(x, y, z)$ , respectively. In this mechanical problem, the Cartesian vessel wall displacement field and strain components are of interest. The assumption of plane strain was made (in the  $(r, \varphi)$ -plane) because the vessel length is at least of the same order of magnitude as its radial dimension.

The two elastic media are assumed to be incompressible and isotropic and are described by the constitutive laws [38]

$$[\sigma]^{(m)} = -p^{(m)} [I] + \frac{2}{3} E^{(m)} [\varepsilon]^{(m)} \quad (\text{A.1})$$

where the  $^{(m)}$  denotes the considered medium ( $m = 1$  for the vascular wall for which  $R_i \leq r \leq R_o$  and  $0 \leq \varphi \leq 2\pi$ , and  $m = 2$  for the embedded tissue for which  $R_o \leq r \leq R_e$  and  $0 \leq \varphi \leq 2\pi$ ). The parameters  $[\sigma]^{(m)}$  and  $[\varepsilon]^{(m)}$  are the stress and strain tensors,  $[I]$  is the identity matrix,  $E^{(m)}$  are the Young's moduli, and  $p^{(m)}$  are the Lagrangian multipliers resulting from the incompressibility of the materials [38] given by the following kinematics constraints:

$$\nabla \cdot \vec{u}^{(m)} = 0 \quad (\text{A.2})$$

where  $\vec{u}^{(m)}$  are unknown displacement vectors. If gravity and inertial forces are neglected, the conditions of local equilibrium are  $\nabla \cdot [\sigma]^{(m)} = \vec{0}$ , or in terms of the displacement vectors

$$\nabla p^{(m)} = \frac{E^{(m)}}{3} \nabla^2 \vec{u}^{(m)}. \quad (\text{A.3})$$

The displacement fields  $\vec{u}^{(m)}$  as well as the stress tensors  $[\sigma]^{(m)}$  must satisfy the following boundary conditions. The blood pressure  $P_b$  is uniform

$$[\sigma]^{(1)} \vec{e}_r = -P_b \vec{e}_r \quad \text{at} \quad r = R_i \quad (\text{A.4})$$

no stresses are applied on the external surface of the surrounded tissue

$$[\sigma]^{(2)} \vec{e}_r = \vec{0} \quad \text{at} \quad r = R_e \quad (\text{A.5})$$

and at the interface between the vessel wall and the surrounded tissue, we must have the continuity of displacement fields and equality of the stress vectors

$$\vec{u}^{(1)} = \vec{u}^{(2)} \quad \text{at} \quad r = R_o \quad (\text{A.6})$$

$$[\sigma]^{(1)} \vec{e}_r = [\sigma]^{(2)} \vec{e}_r \quad \text{at} \quad r = R_o. \quad (\text{A.7})$$

Due to the symmetry of the mechanical problem and because the two media are incompressible, the displacement solutions are

$$\vec{u}^{(1)}(r) = \vec{u}^{(2)}(r) = \frac{K}{r} \vec{e}_r \quad (\text{A.8})$$

where  $K$  is a constant. The equilibrium conditions [see (A.3)] are satisfied only if the two Lagrangian terms  $p^{(1)}$  and  $p^{(2)}$  are constant. At the end, the three unknowns of the problem ( $K$ ,  $p^{(1)}$ ,  $p^{(2)}$ ) are found by using the boundary conditions given by (A.4), (A.5), and (A.7). Hence, for the value of  $K$ , we have

$$K = \frac{3}{2} P_b \left[ E^{(1)} \left( \frac{1}{R_i^2} - \frac{1}{R_o^2} \right) - E^{(2)} \left( \frac{1}{R_o^2} - \frac{1}{R_e^2} \right) \right]^{-1}. \quad (\text{A.9})$$

In the particular case of a thick-wall cylindrical blood vessel embedded in an infinite medium, the new value of  $K$  is obtained from the limit  $K_\infty = \lim_{R_e \rightarrow \infty} K$ , and is given by

$$K_\infty = \frac{3}{2} P_b \left[ E^{(1)} \left( \frac{1}{R_i^2} - \frac{1}{R_o^2} \right) + \frac{E^{(2)}}{R_o^2} \right]^{-1}. \quad (\text{A.10})$$



So, the needed Cartesian components of the displacement vectors and strain tensors are

$$u_x(x, y) = K_\infty \frac{x}{x^2 + y^2} \quad (\text{A.11})$$

$$u_y(x, y) = K_\infty \frac{y}{x^2 + y^2} \quad (\text{A.12})$$

$$\varepsilon_{xx}(x, y) = \frac{\partial u_x}{\partial x} = K_\infty \frac{y^2 - x^2}{(x^2 + y^2)^2} \quad (\text{A.13})$$

$$\varepsilon_{yy}(x, y) = \frac{\partial u_y}{\partial y} = K_\infty \frac{x^2 - y^2}{(x^2 + y^2)^2} \quad (\text{A.14})$$

$$\varepsilon_{xy}(x, y) = \frac{1}{2} \left( \frac{\partial u_x}{\partial y} + \frac{\partial u_y}{\partial x} \right) = -2K_\infty \frac{xy}{(x^2 + y^2)^2}. \quad (\text{A.15})$$

## REFERENCES

- [1] J. Ophir, E. I. Céspedes, H. Ponnekanti, Y. Yazdi, and X. Li, "Elastography: A quantitative method for imaging the elasticity in biological tissues," *Ultrason. Imag.*, vol. 13, no. 2, pp. 111–134, 1991.
- [2] B. S. Garra, E. I. Céspedes, J. Ophir, S. R. Spratt, R. A. Zuurbier, C. M. Magnant, and M. F. Pennanen, "Elastography of breast lesions: Initial clinical results," *Radiology*, vol. 202, no. 1, pp. 79–86, 1997.
- [3] E. I. Céspedes, J. Ophir, H. Ponnekanti, and N. F. Maklad, "Elastography: Elasticity imaging using ultrasound with application to muscle and breast in vivo," *Ultrason. Imag.*, vol. 15, no. 2, pp. 73–88, 1993.
- [4] A. Lorenz, H. J. Sommerfeld, M. Garcia-Schurmann, S. Philippou, T. Senge, and H. Ermert, "A new system for the acquisition of ultrasonic multicompression strain images of the human prostate in vivo," *IEEE Trans. Ultrason., Ferroelect., Freq. Contr.*, vol. 46, pp. 1147–1154, May 1999.
- [5] A. Pesavento, A. Lorenz, S. Siebers, and H. Ermert, "New real-time strain imaging concepts using diagnostic ultrasound," *Phys. Med. Biol.*, vol. 45, no. 6, pp. 1423–1435, 2000.
- [6] L. Soualmi, M. Bertrand, R. Mongrain, and J. C. Tardif, "Forward and inverse problems in endovascular elastography," in *Acoustical Imaging*, S. Lees and L. A. Ferrari, Eds. New York: Plenum, 1997, pp. 203–209.
- [7] C. L. de Korte, E. I. Céspedes, A. F. W. Van der Steen, and C. T. Lancee, "Intravascular elasticity imaging using ultrasound – Feasibility studies in phantoms," *Ultrasound Med. Biol.*, vol. 23, no. 5, pp. 735–746, 1997.
- [8] L. K. Ryan and F. S. Foster, "Ultrasonic measurement of differential displacement strain in a vascular model," *Ultrason. Imag.*, vol. 19, no. 1, pp. 19–38, 1997.
- [9] B. M. Shapo, J. R. Crowe, A. R. Skovoroda, M. J. Eberle, N. A. Cohn, and M. O'Donnell, "Displacement and strain imaging of coronary arteries with intraluminal ultrasound," *IEEE Trans. Ultrason., Ferroelect., Freq. Contr.*, vol. 43, pp. 234–246, Feb. 1996.
- [10] B. M. Shapo, J. R. Crowe, R. Erkamp, S. Y. Emelianov, M. J. Eberle, and M. O'Donnell, "Strain imaging of coronary arteries with intraluminal ultrasound: Experiments on an inhomogeneous phantom," *Ultrason. Imag.*, vol. 18, no. 3, pp. 173–191, 1996.
- [11] E. Brusseau, J. Fromageau, G. Finet, P. Delachartre, and D. Vray, "Axial strain imaging of intravascular data: Results on polyvinyl alcohol cryogel phantoms and carotid artery," *Ultrasound Med. Biol.*, vol. 27, no. 12, pp. 1631–1642, 2001.
- [12] C. L. de Korte, A. F. W. Van der Steen, E. I. Céspedes, and G. Pasterkamp, "Intravascular ultrasound elastography in human arteries: Initial experience in vitro," *Ultrasound Med. Biol.*, vol. 24, no. 3, pp. 401–408, 1998.
- [13] C. L. de Korte, G. Pasterkamp, A. F. W. Van der Steen, H. A. Woutman, and N. Bom, "Characterization of plaque components with intravascular ultrasound elastography in human femoral and coronary arteries in vitro," *Circulation*, vol. 102, no. 6, pp. 617–623, 2000.
- [14] M. Wan, Y. Li, J. Li, Y. Cui, and X. Zhou, "Strain imaging and elasticity reconstruction of arteries based on intravascular ultrasound video images," *IEEE Trans. Biomed. Eng.*, vol. 48, pp. 116–120, Jan. 2001.
- [15] C. L. de Korte, A. F. W. Van der Steen, E. I. Céspedes, G. Pasterkamp, S. G. Carlier, F. Mastik, A. H. Schoneveld, P. W. Serruys, and N. Bom, "Characterization of plaque components and vulnerability with intravascular ultrasound elastography," *Phys. Med. Biol.*, vol. 45, no. 6, pp. 1465–1475, 2000.
- [16] R. L. Maurice and M. Bertrand, "Lagrangian speckle model and tissue-motion estimation – Theory," *IEEE Trans. Med. Imag.*, vol. 18, pp. 593–603, July 1999.
- [17] —, "Tissue strain estimation using a Lagrangian speckle model," in *Acoustical Imaging*, R. S. Lees and L. A. Ferrari, Eds. New York: Plenum, 1997, pp. 113–117.
- [18] P. Chaturvedi, M. F. Insana, and T. J. Hall, "2-D companding for noise reduction in strain imaging," *IEEE Trans. Ultrason., Ferroelect., Freq. Contr.*, vol. 45, pp. 179–191, Jan. 1998.
- [19] —, "Testing the limitations of 2-D companding for strain imaging using phantoms," *IEEE Trans. Ultrason., Ferroelect., Freq. Contr.*, vol. 45, pp. 1022–1031, July 1998.
- [20] F. Kallel and M. Bertrand, "Speckle motion artifact under tissue rotation," *IEEE Trans. Ultrason., Ferroelect., Freq. Contr.*, vol. 41, pp. 105–122, Jan. 1994.
- [21] R. L. Maurice and M. Bertrand, "Speckle-motion artifact under tissue shearing," *IEEE Trans. Ultrason., Ferroelect., Freq. Contr.*, vol. 46, pp. 584–594, May 1999.
- [22] K. Levenberg, "A method for the solution of certain nonlinear problems in least-squares," *Q. Appl. Math.*, vol. 2, no. 2, pp. 164–168, 1944.
- [23] D. W. Marquardt, "An algorithm for least-squares estimation of nonlinear parameters," *J. SIAM*, vol. 11, no. 2, pp. 431–441, 1944.
- [24] B. Le Mehaute, *An Introduction to Hydrodynamics and Water Waves*. New York: Springer-Verlag, 1976, pp. 18–20.
- [25] J. O. Hinze, *Turbulence*, 2 ed. New York: McGraw-Hill, 1975, pp. 1–781.
- [26] J. Ophir, S. K. Alam, B. Garra, F. Kallel, E. Konofagou, T. Krouskop, and T. Varghese, "Elastography: Ultrasonic estimation and imaging of the elastic properties of tissues," *Proc. Inst. Mech. Eng. Part H – J. Eng. Med.*, vol. 213, no. H3, pp. 203–233, 1999.
- [27] *Ansys Theory Reference*, 11th ed. SAS IP Inc., 1999.
- [28] G. E. Mase, *Theory and Problems of Continuum Mechanics*. New York: McGraw-Hill, 1970, Schaum's Outline Series.
- [29] E. S. da Silva, A. J. Rodrigues, E. M. C. de Tolosa, C. J. Rodrigues, G. V. B. do Prado, and J. C. Nakamoto, "Morphology and diameter of infrarenal aortic aneurysms: A prospective autopsy study," *Cardiovasc. Surg.*, vol. 8, no. 7, pp. 526–532, 2000.
- [30] R. C. Darling, C. R. Messina, D. C. Brewster, and L. W. Ottinger, "Autopsy study of unoperated abdominal aortic aneurysms. The case for early resection," *Circulation*, vol. 56, no. Suppl. 3, pp. 161–164, 1977.
- [31] R. C. Darling, "Ruptured arteriosclerotic abdominal aortic aneurysms. A pathologic and clinical study," *Amer. J. Surg.*, vol. 119, no. 4, pp. 397–401, 1970.
- [32] K. Ouriel, R. M. Green, C. Donayre, C. K. Shortell, J. Elliott, and J. A. DeWeese, "An evaluation of new methods of expressing aortic aneurysm size: Relationship to rupture," *J. Vasc. Surg.*, vol. 15, no. 1, pp. 12–20, 1992.
- [33] M. Eriksen, "Noninvasive measurement of arterial diameters in humans using ultrasound echoes with prefiltered waveforms," *Med. Biol. Eng. Comput.*, vol. 25, no. 2, pp. 189–194, 1987.
- [34] S. H. K. The, E. J. Gussenhoven, H. Pieterman, M. A. Van Borden, W. Li, J. R. Roelandt, P. de Feyter, and H. Van Urk, "Assessment of regional vascular distensibility in diseased iliofemoral arteries by intravascular ultrasound," *Ultrasound Med. Biol.*, vol. 21, no. 1, pp. 17–24, 1995.
- [35] B. Heintz, F. Walkenhorst, T. Gillesen, R. Dorr, W. Krebs, J. Vondahl, and P. Hanrath, "In vivo characterization of segmental elastic properties of the aortic tree by intravascular ultrasound," *Cardiol. Elderly*, vol. 2, no. 2, pp. 127–132, 1994.
- [36] S. E. Greenwald, J. E. Moore, A. Rachev, T. P. C. Kane, and J.-J. Meister, "Experimental investigation of the distribution of residual strains in the artery wall," *J. Biomechan. Eng.*, vol. 119, pp. 438–444, 1997.
- [37] Y. Matsumoto, T. Honda, M. Hamada, T. Toyama, H. Matsuoka, and K. Hiwada, "Evaluation of short axial blood flow pattern in thoracic descending aorta by use of tagging cine magnetic resonance," *J. Vasc. Diseases*, vol. 45, no. 11, pp. 917–922, 1994.
- [38] A. E. Green and W. Zerna, *Theoretical Elasticity*, 2nd ed. New York: Dover, 1968, pp. 113–144.